arXiv:1410.0655v1 [cond-mat.mes-hall] 2 Oct 2014

Electrostatic Coupling between Two Surfaces of a Topological Insulator Nanodevice

Valla Fatemi,[1,*] Benjamin Hunt,[1] Hadar Steinberg,[2,1] Stephen L. Eltinge,[1] Fahad Mahmood,[1] Nicholas P. Butch,[3,4,5] Kenji Watanabe,[6] Takashi Taniguchi,[6] Nuh Gedik,[1] Ray Ashoori,[1] and Pablo Jarillo-Herrero[1]

[1] *Department of Physics, Massachusetts Institute of Technology, Cambridge, Massachusetts 02139, USA*
[2] *Racah Institute of Physics, The Hebrew University, Jerusalem 91904, Israel*
[3] *Center for Neutron Research, National Institute of Standards and Technology, 100 Bureau Drive, MS 6100 Gaithersburg, MD 20899, USA*
[4] *Center for Nanophysics and Advanced Materials, Department of Physics, University of Maryland, College Park, MD 20742*
[5] *Lawrence Livermore National Laboratory 7000 East Avenue, Livermore, CA 94550, USA*
[6] *Advanced Materials Laboratory, National Institute for Materials Science, 1-1 Namiki, Tsukuba 305-0044, Japan*

(Dated: October 3, 2014)

We report on electronic transport measurements of dual-gated nano-devices of the low-carrier density topological insulator $Bi_{1.5}Sb_{0.5}Te_{1.7}Se_{1.3}$. In all devices the upper and lower surface states are independently tunable to the Dirac point by the top and bottom gate electrodes. In thin devices, electric fields are found to penetrate through the bulk, indicating finite capacitive coupling between the surface states. A charging model allows us to use the penetrating electric field as a measurement of the inter-surface capacitance C_{TI} and the surface state energy-density relationship $\mu(n)$, which is found to be consistent with independent ARPES measurements. At high magnetic fields, increased field penetration through the surface states is observed, strongly suggestive of the opening of a surface state band gap due to broken time-reversal symmetry.

PACS numbers: 73.20.Fz, 72.15.Rn, 73.25.+i,85.30.Tv,84.37.+q

Three dimensional topological insulators (3D TIs) have been undergoing intense theoretical and experimental research on the properties of their unique surface states [1, 2]. The presence of bulk carriers has hampered experimental progress, so a variety of crystal growth [3–8] and in-situ charge displacement techniques [9–13] have been applied to suppress bulk conductivity. For example, quaternary TI materials of the form $Bi_{2-x}Sb_xTe_{3-y}Se_y$ have a significantly suppressed bulk contribution to transport, reaching large bulk resistivities and insulating-like temperature dependence [6, 14, 15]. Furthermore, exfoliation or growth of thin crystals has been used to achieve surface-dominated transport [7, 8, 12, 16, 17]. However, amid the extensive experimental effort on TI device transport, there is no study reporting independent control over the density of both the upper and lower surface states in a single TI device. A full understanding of transport phenomena in TIs, such as the quantum Hall [18, 19] and Josephon effects [20–22], will require independent tuning of the density of each surface state. Additionally, proposals for topological exciton condensates explicitly require fine tuning the density of both surfaces [23], and finite displacement fields from two gates can affect the quantum anomalous Hall effect in TI-based systems [24, 25].

In this Letter, we report electronic transport measurements of exfoliated $Bi_{1.5}Sb_{0.5}Te_{1.7}Se_{1.3}$ (BSTS) nanodevices with top and bottom gate electrodes. We show for the first time that the chemical potential of the upper and lower surface states can be controlled independently, resulting in different resistance peaks when either surface chemical potential crosses the Dirac point. For thin devices, we find signatures of finite capacitive coupling between the surface states, consistent with fully depleted bulk states. We explain the data through a charging model which incorporates the finite density of states of the surface bands. Using angle-resolved photoemission spectroscopy (ARPES) as a control measurement of the surface state, this model allows us to measure the chemical potential μ and charge density n of a topological surface state as well as the inter-surface capacitance C_{TI}. At high magnetic fields, increased field penetration through the surface states is observed, strongly suggestive of the opening of a surface state band gap.

BSTS was prepared by melting high purity samples of the constituent elements in a sealed quartz ampoule under inert atmosphere. Sample structure was confirmed by x-ray powder diffraction, and large single crystals showed similar bulk transport behavior to previous reports [6]. Static ARPES shows that the chemical potential is inside the bulk band gap and that the Dirac point energy is above the bulk valence band edge (see SM [26]). Pump-probe time-resolved ARPES (TrARPES) allows access to unoccupied states as shown in Fig. 1b [27, 28]. The Fermi velocity near the Dirac point is $v_F \approx 3.2 \times 10^5$m/s, and the band gap at room temperature is $E_g \approx 240$ meV. Note that the surface state dispersion is strongly electron-hole asymmetric. These data are consistent with previous experiments [14, 29].

Thin flakes for transport studies were obtained by mechanical exfoliation onto a doped silicon wafer with a 285nm thick thermal SiO_2 surface layer that serves as the bottom gate electrode and dielectric, respectively. A thin layer of hexagonal boron nitride (h-BN) was mechan-

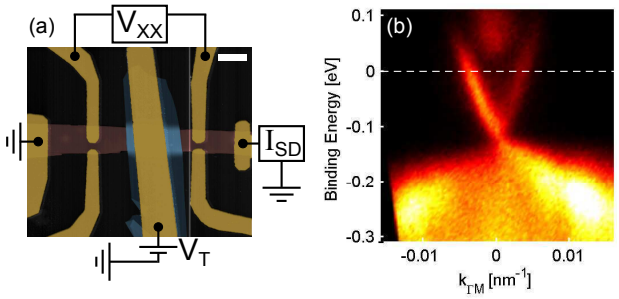


FIG. 1. (Color online) (a) Colorized AFM image of device A, including schematic circuit elements describing the transport measurement. Red is BSTS, blue is h-BN, and gold is Ti/Au (contacts and gate electrode). The scale bar is 2 microns. (b) TrARPES measurement of a BSTS crystal. The white line indicates the chemical potential.

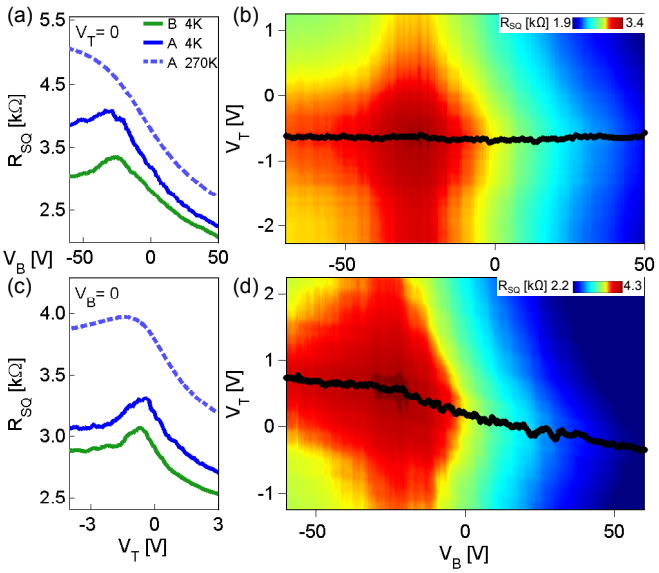


FIG. 2. (Color online) Gate-dependence of the resistivity of devices A and B. (a) Bottom gate dependence of resistivity at $V_T = 0$ at low temperature (blue, green) and 270K (dashed) from cooldown 2. (c) Top gate dependence of resistivity at $V_B = 0$ at low temperature (blue, green) and 270K (dashed) from cooldown 2. (b,d) 2D map of resistivity while modulating both gate electrodes for devices B and A, respectively, from cooldown 1. The black dots track the location of the upper surface R_{peak} at each V_B.

ically transferred on top to serve as the top gate dielectric [30]. Thermally evaporated Ti/Au layers were used to make ohmic contacts and top gate electrodes. Atomic Force Microscopy was used to determine the thickness of the BSTS and h-BN layers. For all data presented here, a four-probe voltage measurement was used determine the 2D resistivity. Here we report results measured on BSTS devices of different thicknesses: device A is 42 nm, and device B is 82 nm. The behavior of device A was reproduced in a third device [26]. All three devices were fabricated from flakes from the same exfoliation, and therefore from the same region of the bulk crystal. Fig. 1a, shows an AFM image of device A.

On devices A and B, both the top and bottom gates easily tune the device through a resistance peak (R_{peak}) by adjusting the applied voltages V_T and V_B, respectively, as shown in Fig. 2a-b. R_{peak} is associated with a minimum in carrier density (i.e. the surface Dirac point), as confirmed via the Hall effect [26]. Interestingly, the top-gate R_{peak} is observable up to room temperature; in contrast, for the bottom gate $R(V_B)$ changes into a broad S-shape, consistent with gating studies of other TIs using SiO_2 gate dielectrics [7, 10, 17]. The disappearance of a distinct resistance peak in the limit of strong disorder was predicted by recent theories for TI surface states with electron-hole asymmetry [31], suggesting that the difference in the field-effect behavior may be related to the disorder profile at the interface. Strong differences in the disorder profile at SiO_2 and h-BN interfaces have been observed in graphene [32].

Two-dimensional maps of the resistivity with respect to both top and bottom gate voltage reveal a distinct difference in the behavior of devices A and B, shown in Fig. 2d and 2c, respectively. The black dots identify V_T, the top gate voltage at which R_{peak} is found, at each V_B. We associate V_{peak} with charge neutrality of the upper surface state: $n_U = 0$. For device B, V_{peak} is independent of V_B, demonstrating no capacitive coupling between the upper surface and the bottom gate electrode. The fact that thicker devices do not have this capacitive coupling suggests that mobile bulk electronic states exist in the interior. By contrast, V_{peak} in device A is dependent on V_B. The observed relationship $V_{peak}(V_B)$ means that there exists a finite and *non-constant* capacitive coupling between the upper surface and the bottom gate. This capacitive coupling requires field penetration through the lower surface state and the interior of the thinner crystal, which fail to completely screen electric fields. The contrasting gating behavior of the devices is corroborated by the temperature dependence of their resistivities (see SM [26]). We also note that while dual-gated TI devices have been previously reported [12, 33], the devices reported here are unique in that the two surface states are tuned independently and separately observed.

Here we focus on the capacitive coupling between the bottom gate and the upper surface in the thin crystal, and data regarding coupling of the top gate and lower surface are presented in the SM [26]. The slope of $V_{peak}(V_B)$ is a measure of the ratio of the capacitive coupling of the bottom and top gates to the upper surface, which includes partial screening of electric fields by the lower surface state. At $V_B \sim -20$ V the slope of $V_{peak}(V_B)$ and the resistance of the lower surface are simultaneously at a maximum, i.e. near the Dirac point (see Fig. 3b). This is consistent with a minimum in the

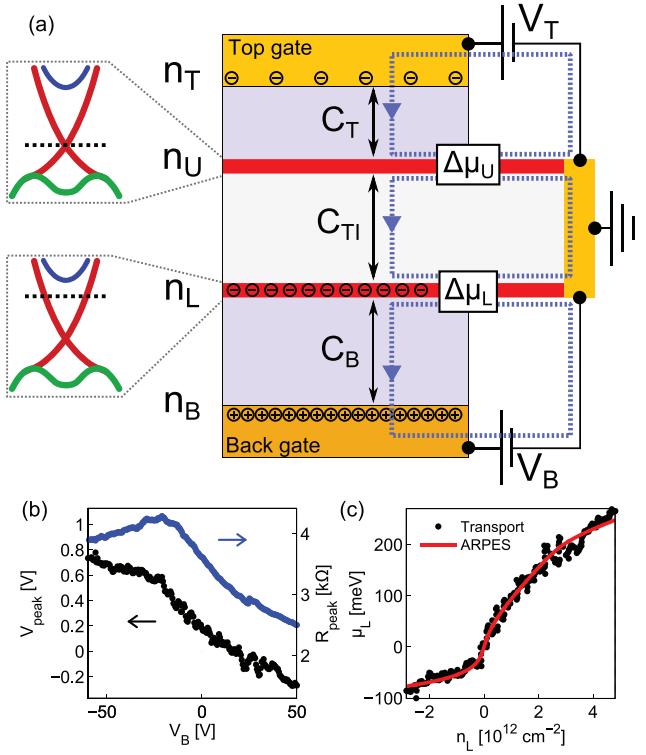


FIG. 3. (Color online) (a) Schematic of the charging model used in this study with important parameters labeled. For comparison to the experiment, the upper surface state is kept at charge neutrality while charge is distributed between the lower surface state and the gate electrodes. Three voltage loops indicated by the blue dashed lines are used in deriving the charging model. (b) The position of the upper surface R_{peak} as a function of both gate voltages $V_{peak}(V_B)$ (left, black dots), and the resistivity at those gate voltages R_{peak} (right, blue), extracted from Fig. 2d. (c) The fit of the energy-density relationship as derived from ARPES (red line) and from $V_{peak}(V_B)$ (black dots).

screening effectiveness of the lower surface state at the Dirac point. Understanding this behavior quantitatively requires a detailed charging model, which we discuss below.

By considering the BSTS surface states as a grounded pair of 2D electronic states, the general gating behavior can be understood via a charging model construction originally developed for parallel graphene layers [34]. This model is schematically represented in Fig. 3a, where the important quantities are the applied gate voltages (V_T, V_B), the geometric capacitances per unit area of the gates (C_B, C_T), the inter-surface capacitance per unit area (C_{TI}), the charge densities of the gate electrodes (n_T, n_B), and the charge density and chemical potentials of the lower (n_L, μ_L) and upper (n_U, μ_U) surface states. Four coupled equations completely describe the charging of the system: one from charge neutrality, and three from Faraday's law, which restricts the sum of voltage drops around a loop to equal zero, which includes the change in chemical potential of the surface states $\Delta\mu_j = \mu_j - \mu_j^0$, where μ_j^0 is the initial Fermi energy relative to the Dirac point for surface state $j = U, L$. A detailed derivation is provided in the SM [26]. For this study, we are interested in the condition that the chemical potential at the upper surface is at the Dirac point. By setting $n_U = 0$ and $\mu_U = 0$, a useful pair of equations can be derived:

$$\mu_L = -\frac{C_T}{C_{TI}} eV_T' \tag{1}$$

$$\frac{1}{C_B} en_L = V_B' + \left(\frac{1}{C_B} + \frac{1}{C_{TI}}\right) C_T V_T', \tag{2}$$

where $V_{T,B}' = V_{T,B} - V_{T,B}^0$, and $V_{T,B}^0$ are constants that depend on the initial densities and chemical potentials of the two surfaces (see SM [26]). Equations 1 and 2 serve as a linear transformation from a trajectory in gate voltage space (Fig. 3b) to a relationship between chemical potential and density for the lower surface state (Fig. 3c).

Experimentally, three unknowns remain: the inter-surface capacitance C_{TI} and the initial offset carrier densities of the upper and lower surfaces $n_{L,U}^0$. To constrain these parameters, an independent measurement of $\mu(n)$ is required. ARPES measurements of the surface state band structure can be easily converted to a model for $E(n)$, including an explicit treatment of the bulk states [26]. A three-parameter least-squares fit between the transformation of the transport data and the ARPES model is performed and shown in Fig. 3c [26]. The inter-layer capacitance from this fit is $C_{TI} = 740 \pm 20$ nF/cm^2, corresponding to an effective bulk permittivity of $\kappa_{TI} \approx 32$, comparable to values for similar compounds [35–37]. The initial electron densities of the upper and lower surface states are found to be $n_U^0 \approx -0.1 \times 10^{12} cm^{-2}$ and $n_L^0 \approx 1.2 \times 10^{12} cm^{-2}$, which agrees well with values simply calculated from the magnitude of V_T and V_B necessary to reach the resistance peaks.

It is important to note that C_{TI} can be affected in a few ways. For example, localized electronic states could polarize, increasing C_{TI}. As another possibility, low-density, poorly conducting bulk states could weakly screen electric fields, reducing C_{TI}. However, in the thin limit the surface states should efficiently screen charged bulk impurities, resulting in an absence of charged puddles of bulk states at charge neutrality for crystals of thickness $\lesssim 70$ nm [38]. This length scale is consistent with the observation that device B (82 nm thick) appears to have conducting states screening the two surfaces from each other.

We now turn to the behavior of the thin device in high magnetic fields. The Hall mobility of this sample is low, of order 200 cm^2/(Vs); as a result, no evidence of Landau levels is found, and a clear R_{peak} remains. Nevertheless, the charging behavior of the device changes significantly at finite field. Fig. 4a shows $V_{T,peak}(V_B)$ of the upper surface R_{peak} at $B = 0$ T and 8 T. V_{peak} is affected

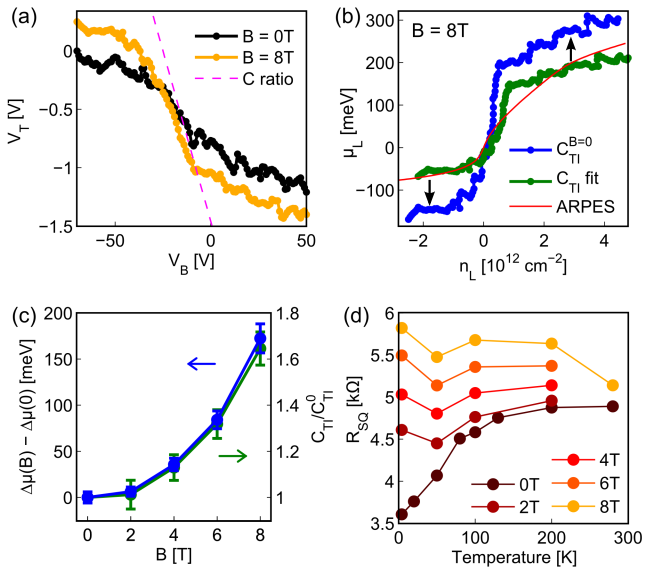


FIG. 4. Effect of high magnetic fields on the transport data. (a) $V_{peak}(V_B)$ at 0T and 8T from cooldown 2. For comparison, the dashed pink line would be the gate-gate dependence if the lower surface has no electronic states, given by a ratio of geometric capacitances: C ratio $= -\frac{1}{C_T}\frac{C_B C_{TI}}{(C_B+C_{TI})}$. The transport data approaches this slope at 8T. (b) The extracted energy-density relationship of the lower surface state at 8T for the case of fixed inter-surface capacitance $C_{TI} = C^0_{TI}$ (blue) and when using C_{TI} as a fit parameter (green) to the zero-field density of states (ARPES model, red curve). Arrows indicate increase in the total chemical potential change assuming fixed C_{TI}. (c) The difference in the total change of the chemical potential of the lower surface with magnetic field (blue, left axis, error bars are the standard deviation of possible values) and the best fit C_{TI} as a function of magnetic field (green, right axis, error bars are 90% confidence intervals). (d) The temperature dependence of the resistivity at different magnetic fields and when both surfaces are at charge neutrality.

by V_B much more strongly at 8T. Assuming C_{TI} does not change, equations 1 and 2 can be applied without changing parameters, as shown in Fig. 4b (blue dots). For the same total change in charge density, the total chemical potential change of the lower surface is about 60% larger. More precisely, the chemical potential appears to change more rapidly at low carrier densities, indicating a distinctly smaller thermodynamic density of states. Fig. 4c (left axis) shows the difference in total chemical potential change as a function of magnetic field. The energy difference increases roughly quadratically with magnetic field. A possible interpretation is that the surface states develop a band gap that forms as a result of breaking time-reversal symmetry. While a non-linear magnetic field dependence would naively rule out a Zeeman-induced band gap, disorder will mask this effect at low fields when the gap is small [38], causing a non-linear increase in the apparent gap in the density of states. Detailed Shubnikov-de-Haas analysis of similar TI materials estimate a surface g-factor in the range 40 to 80 [39], which would be too small to explain this effect, although the g-factor has not yet been measured for this particular compound.

We further observe that the temperature dependence of resistivity also changes significantly at high magnetic fields. In Figure 4d, the temperature dependence of resistivity when both surfaces are at charge neutrality changes from metallic-like at zero magnetic field to non-metallic at high magnetic field, suggestive of a possible metal-insulator transition. This is consistent with the formation of a gap in the surface states with a high level of disorder. Similar non-metallic resistivity vs temperature curves were observed in bilayer graphene studies with similar band gaps in the high-disorder limit [40].

However, we cannot rule out the possibility of an inter-surface magneto-capacitance. Restricting the model such that the total chemical potential change is the same as at zero magnetic field (i.e. a field-independent *average* density of states, see green curve in Fig. 4b), we find that C_{TI} must increase in magnetic field to compensate (Fig. 4c, right axis). C_{TI} increases in a similar way as the chemical potential difference because $\Delta\mu_L \cdot C_{TI} \propto \Delta V_T$, as in equation 1. The raw bulk permittivity cannot explain this change, because the optical phonon spectra of related TI compounds show little change at similar magnetic fields [41, 42]. Electronic contributions to C_{TI} such as those mentioned earlier (polarizable localized states or weakly screening bulk states) could be modified by a magnetic field. In the supplement we show evidence that the effects of temperature and magnetic field separately affect C_{TI} and $\mu_L(n)$, respectively [26], further suggesting that the magnetic field is modifying the density of states and not causing a magneto-capacitive effect.

In summary, exfoliated nanoflakes of BSTS are of sufficiently low total carrier density for both the upper and lower surface state densities to be independently modulated by electrostatic gates and for electric fields to penetrate through the bulk. Utilizing a model that captures the charging of the system, we measure the inter-surface capacitance C_{TI} as well as the energy-density relationship $\mu(n)$ of the surface states, which agrees well with independent ARPES measurements. At high magnetic fields, increased field penetration is observed, strongly suggestive of band gap opening in the lower surface state.

This work was partly supported by the DOE, Basic Energy Sciences Office, Division of Materials Sciences and Engineering, under award de-sc0006418 (VF, SE, HS, and PJH), by the Gordon and Betty Moore Foundation grant GBMF2931 and the STC Center for Integrated Quantum Materials, NSF grant DMR-1231319 (BH and RCA), and by an MIT MRSEC Initiative under NSF award DMR-0819762 (FM and NG). This work made use of the Materials Research Science and Engineering Center Shared Experimental Facilities supported by NSF under award DMR-0819762. Sample fabrica-

tion was performed partly at the Harvard Center for Nanoscale Science supported by the NSF under grant no. ECS-0335765. Sample synthesis and initial characterization were performed under LDRD (Tracking Code 12-ERD-013) at Lawrence Livermore National Laboratory (LLNL). LLNL is operated by Lawrence Livermore National Security, LLC, for the US Department of Energy, National Nuclear Security Administration, under Contract No. DE-AC52-07NA27344. We thank A. Stern, Y. Baum, K. Burch, D. Drew, B. Skinner, A. Frenzel, and J.D. Sanchez-Yamagishi for discussions and J. R. Jeffries for performing x-ray diffraction measurements.

* vfatemi@mit.edu

[1] M. Z. Hasan and C. L. Kane, Rev. Mod. Phys. **82**, 3045 (2010).
[2] X.-L. Qi and S.-C. Zhang, Rev. Mod. Phys. **83**, 1057 (2011).
[3] Y. S. Hor, A. Richardella, P. Roushan, Y. Xia, J. G. Checkelsky, A. Yazdani, M. Z. Hasan, N. P. Ong, and R. J. Cava, Phys. Rev. B **79**, 195208 (2009).
[4] J. Zhang, C.-Z. Chang, Z. Zhang, J. Wen, X. Feng, K. Li, M. Liu, K. He, L. Wang, X. Chen, Q.-K. Xue, X. Ma, and Y. Wang, Nat Commun **2**, 574 (2011).
[5] Z. Ren, A. A. Taskin, S. Sasaki, K. Segawa, and Y. Ando, Phys. Rev. B **82**, 241306 (2010).
[6] Z. Ren, A. A. Taskin, S. Sasaki, K. Segawa, and Y. Ando, Phys. Rev. B **84**, 165311 (2011).
[7] D. Kong, Y. Chen, J. J. Cha, Q. Zhang, J. G. Analytis, K. Lai, Z. Liu, S. S. Hong, K. J. Koski, S.-K. Mo, Z. Hussain, I. R. Fisher, Z.-X. Shen, and Y. Cui, Nat Nano **6**, 705 (2011).
[8] P. Gehring, B. F. Gao, M. Burghard, and K. Kern, Nano Lett. **12**, 5137 (2012).
[9] H. Steinberg, D. R. Gardner, Y. S. Lee, and P. Jarillo-Herrero, Nano Lett. **10**, 5032 (2010).
[10] J. G. Checkelsky, Y. S. Hor, R. J. Cava, and N. P. Ong, Phys. Rev. Lett. **106**, 196801 (2011).
[11] H. Yuan, H. Liu, H. Shimotani, H. Guo, M. Chen, Q. Xue, and Y. Iwasa, Nano Lett. **11**, 2601 (2011).
[12] D. Kim, S. Cho, N. P. Butch, P. Syers, K. Kirshenbaum, S. Adam, J. Paglione, and M. S. Fuhrer, Nat Phys **8**, 459 (2012).
[13] K. Segawa, Z. Ren, S. Sasaki, T. Tsuda, S. Kuwabata, and Y. Ando, Phys. Rev. B **86**, 075306 (2012).
[14] T. Arakane, T. Sato, S. Souma, K. Kosaka, K. Nakayama, M. Komatsu, T. Takahashi, Z. Ren, K. Segawa, and Y. Ando, Nat. Comm. **3**, 636 (2012).
[15] A. A. Taskin, Z. Ren, S. Sasaki, K. Segawa, and Y. Ando, Phys. Rev. Lett. **107** (2011), 10.1103/PhysRevLett.107.016801.
[16] J. Lee, J. Park, J.-H. Lee, J. S. Kim, and H.-J. Lee, Phys. Rev. B **86** (2012), 10.1103/PhysRevB.86.245321.
[17] B. Xia, P. Ren, A. Sulaev, P. Liu, S.-Q. Shen, and L. Wang, Phys. Rev. B **87**, 085442 (2013).
[18] D. Tilahun, B. Lee, E. M. Hankiewicz, and A. H. MacDonald, Phys. Rev. Lett. **107**, 246401 (2011).
[19] O. Vafek, Phys. Rev. B **84**, 245417 (2011).
[20] J. R. Williams, A. J. Bestwick, P. Gallagher, S. S. Hong, Y. Cui, A. S. Bleich, J. G. Analytis, I. R. Fisher, and D. Goldhaber-Gordon, Phys. Rev. Lett. **109**, 056803 (2012).
[21] M. Veldhorst, M. Snelder, M. Hoek, T. Gang, V. K. Guduru, X. L. Wang, U. Zeitler, W. G. van der Wiel, A. A. Golubov, H. Hilgenkamp, and A. Brinkman, Nat Mater **11**, 417 (2012).
[22] L. P. Rokhinson, X. Liu, and J. K. Furdyna, Nat Phys **8**, 795 (2012).
[23] B. Seradjeh, J. E. Moore, and M. Franz, Phys. Rev. Lett. **103**, 066402 (2009).
[24] R. Yu, W. Zhang, H.-J. Zhang, S.-C. Zhang, X. Dai, and Z. Fang, Science **329**, 61 (2010), PMID: 20522741.
[25] C.-Z. Chang, J. Zhang, X. Feng, J. Shen, Z. Zhang, M. Guo, K. Li, Y. Ou, P. Wei, L.-L. Wang, Z.-Q. Ji, Y. Feng, S. Ji, X. Chen, J. Jia, X. Dai, Z. Fang, S.-C. Zhang, K. He, Y. Wang, L. Lu, X.-C. Ma, and Q.-K. Xue, Science **340**, 167 (2013).
[26] "See supplemental material at [url] for additional arpes data, data on a third device, hall effect data, gating behavior of conductance fluctuations, a detailed derivation of the charging model, and additional temperature- and magnetic field-dependence data.".
[27] J. A. Sobota, S. Yang, J. G. Analytis, Y. L. Chen, I. R. Fisher, P. S. Kirchmann, and Z.-X. Shen, Phys. Rev. Lett. **108**, 117403 (2012).
[28] Y. H. Wang, D. Hsieh, E. J. Sie, H. Steinberg, D. R. Gardner, Y. S. Lee, P. Jarillo-Herrero, and N. Gedik, Phys. Rev. Lett. **109**, 127401 (2012).
[29] S. Kim, S. Yoshizawa, Y. Ishida, K. Eto, K. Segawa, Y. Ando, S. Shin, and F. Komori, Phys. Rev. Lett. **112**, 136802 (2014).
[30] C. R. Dean, A. F. Young, I. Meric, C. Lee, L. Wang, S. Sorgenfrei, K. Watanabe, T. Taniguchi, P. Kim, K. L. Shepard, and J. Hone, Nat Nano **5**, 722 (2010).
[31] S. Adam, E. H. Hwang, and S. Das Sarma, Phys. Rev. B **85**, 235413 (2012).
[32] J. Xue, J. Sanchez-Yamagishi, D. Bulmash, P. Jacquod, A. Deshpande, K. Watanabe, T. Taniguchi, P. Jarillo-Herrero, and B. J. LeRoy, Nat Mater **10**, 282 (2011).
[33] J. G. Checkelsky, J. Ye, Y. Onose, Y. Iwasa, and Y. Tokura, Nature Physics **8**, 729 (2012).
[34] S. Kim, I. Jo, D. C. Dillen, D. A. Ferrer, B. Fallahazad, Z. Yao, S. K. Banerjee, and E. Tutuc, Phys. Rev. Lett. **108**, 116404 (2012).
[35] Collaboration: Authors and editors of the volumes III/17E-17F-41C, in *Non-Tetrahedrally Bonded Elements and Binary Compounds I*, Vol. 41C, edited by O. Madelung, U. Rössler, and M. Schulz (Springer-Verlag, Berlin/Heidelberg) pp. 1–4.
[36] J. Petzelt and J. Grigas, Ferroelectrics **5**, 59 (1973).
[37] W. Richter and C. R. Becker, physica status solidi (b) **84**, 619–628 (1977).
[38] B. Skinner, T. Chen, and B. I. Shklovskii, J. Exp. The. Phys. **117**, 579 (2013).
[39] A. A. Taskin and Y. Ando, Phys. Rev. B **84**, 035301 (2011).
[40] J. B. Oostinga, H. B. Heersche, X. Liu, A. F. Morpurgo, and L. M. K. Vandersypen, Nat Mater **7**, 151 (2008).
[41] A. B. Sushkov, G. S. Jenkins, D. C. Schmadel, N. P. Butch, J. Paglione, and H. D. Drew, Phys. Rev. B **82**, 125110 (2010).
[42] A. D. LaForge, A. Frenzel, B. C. Pursley, T. Lin, X. Liu, J. Shi, and D. N. Basov, Phys. Rev. B **81**, 125120 (2010).